Article

Identification of a force-sensing resistor for tactile applications

Mohammad Y Saadeh[1] and Mohamed B Trabia[2]

Abstract

A force-sensing resistor is a conductive polymer that exhibits a decrease in resistance as the force applied at its surface increases. The aim of this study is to identify the characteristics of the force-sensing resistor for use in a refreshable and portable E-Braille device that can assist the blind and visually impaired persons. The force-sensing resistor is placed within a component dynamic testing device that is composed of a linear actuator that can generate different displacement loading profiles and a load cell that measures the applied forces. The system records the voltage, force, and the displacement profiles. Several strategies are used in the identification process. First, the mechanical properties of the force-sensing resistor are experimentally characterized. A second-order mechanical system whose parameters are function of the exciting frequency is created based on the results of this experiment. The performance of this model is evaluated using several test inputs. In an attempt to better identify the force-sensing resistor, alternative higher order linear and nonlinear models, including Hammerstein, Wiener, and Hammerstein–Wiener, are proposed using system identification techniques. The accuracy and robustness of these models are assessed using various loading profiles. The outputs of these models are compared with the experimental results.

Keywords

Force-sensing resistor, blind and visually impaired, refreshable E-Braille device, linear actuator, system identification, Hammerstein, Wiener, dynamic mechanical analysis

Introduction

A force-sensing resistor (FSR) that uses polymer film was recently developed as an alternative to traditional force-sensing devices. FSRs have several advantages including, cost, robustness, wide measurable force range, simplicity of the drive, power consumption, maintenance, and most importantly the very small space they occupy.

Few researchers addressed the repeatability, time drift, hysteresis, and robustness of FSRs. For example, Vecchi et al. (2000) compared the Interlink's FSR (Standard 402) and the Teksan's FlexiForce (A201) sensors and suggested that the FlexiForce had a better repeatability, linearity, and time drift, while the Interlink's product was more robust. Hollinger and Wanderely (2006) proposed another evaluation study of three commercial FSRs. The work considered three types: Interlink FSR (Standard 402), FlexiForce (A201), and LuSense PS3 (Standard 151). It was concluded that the FlexiForce has the highest precision, the highest noise, and the slowest response. However, the FlexiForce's resistance dropped from the nominal value for subsequent tests more than the other products. The authors also recommended using the Interlink or PS3

sensors if the application is composed of large varying forces at high frequencies. Another comparison between the two FSRs was proposed by Lebosse et al. (2008). They found that the FlexiForce exhibited more linear output than the Interlink sensor. Unlike the previous study by Vecchi et al. (2000), they found that the repeatability and the time drift of the Interlink sensor were better than the FlexiForce's.

Several researchers have discussed the problem of calibrating and modeling FSRs. In an attempt to study the biomechanics of the grasp and hand injury rehabilitation, Jensen et al. (1991) used FSRs that are directly attached to the subjects' fingertips. The subjects were asked to pinch a dynamometer for equally spaced force levels while the FSR was calibrated. Regression

[1]Department of Computer Science and Industrial Technology, Southeastern Louisiana University, Hammond, LA, USA
[2]Department of Mechanical Engineering, University of Nevada, Las Vegas, NV, USA

Corresponding author:
Mohamed B Trabia, Department of Mechanical Engineering, University of Nevada, 4505 Maryland Parkway, Las Vegas, NV 89154-4027, USA.
Email: mbt@me.unlv.edu

analysis was then used to describe the force–voltage relation through a second-order polynomial. Vaidyanathan and Wood (1991) also used regression analysis to introduce mathematical model of the FSR using cubic spline interpolation. Birglen and Gosselin (1995) applied static loads to calibrate the resistance response of the FSR using regression analysis. Another attempt to create a linearized FSR region through the implementation of an operational amplifier was proposed (Zehr et al., 1995). They added a proper resistance value in series with the FSR; however, the proposed method failed to account for the significant nonlinearities of the sensor. The focus of the study of Hall et al. (2008) was to calibrate and condition the FSR. First, they conditioned the FSR resistance through an operational amplifier to linearize it around a specific operating region. They assumed that the output voltage is dependent on the loading history, which was represented as a moving integral, to compensate for the hysteresis. Lebosse et al. (2008) also modeled the nonlinear behaviors of two commercial FSRs. The responses were modeled using regression analysis, while the decreases in the FSR's signals over time were modeled as a function of frequency, mean value, and amplitude. Florez and Velasquez (2010) discussed two behaviors of the FSRs: creep and hysteresis. They suggested that creep typically occurs at levels below 0.2 V/s. They derived an expression for the voltage that compensated for any creep effect that is less than the threshold value. They have also suggested that the hysteresis of the sensor can be described by a fourth-order polynomial.

Most of the literature in this field were dedicated either to model the static behavior of the FSR or to assume regional linear response due to dynamic loadings. Neither of these approaches can be generalized, since loadings are dynamic in typical industry applications. In addition, the linear region of an FSR is bounded and cannot provide a convincing description for the entire operational course. In this study, we propose several linear and nonlinear models using two approaches. System identification techniques are used to propose other forms of linear and nonlinear models of the FSR.

Of particular interest to this study is to identify the FSR for implementation in a refreshable and wearable E-Braille reading device (Saadeh et al., 2010; Figures 1 and 2). The device is composed of a refreshable 3×2 tactile array that is printed on an electrotactile display, which is actuated by a miniature direct current (DC) motor that lifts and lowers the electronic board. This linear motion brings the display into contact with the index finger's pulp to start the electronic transmission of data through the electrotactile display. FSR is installed beneath the electrotactile display to measure the contact force felt at the user's finger. The measured force will be used in a feedback control loop to maintain a steady contact pressure between the finger's pulp and the display throughout the reading process. The range of the tactile forces while feeling five different Braille characters was identified experimentally (Saadeh and Trabia, 2010). In this study, we use the range of force that we measured earlier to identify the FSR.

The remainder of this study is outlined as follows: the following section briefly discusses the current FSR technology. Next, an overview of the experimental setup and experimental data conditioning is presented. Then, dynamic mechanical analysis (DMA) test is conducted to build a second-order equivalent system for the FSR whose parameters are functions of the exciting frequency. The next section addresses the use of the system identification techniques to create higher order linear and nonlinear models, including Hammerstein, Wiener, and Hammerstein–Wiener for the FSR. The linear and nonlinear models are then compared, and results and conclusion are presented and discussed.

FSR technology

Several FSR commercial designs exist. The main differences between these designs are in the structure of the layers and the active sensing material used. For instance, the Interlink's FSR is composed of two membranes. One membrane has two sets of electrically distinct interdigitating electrodes. The other membrane holds the printed carbon-based ink of the FSR. A spacer adhesive is applied between the two membranes to hold them together and to ensure that the air gap between them is maintained. A spacer material, like a double-sided stick adhesive, is placed between the two films. Figure 3 shows how the layers of a typical FSR are arranged.

In this study, we provide an experimental approach to identify Interlink's FSR Standard 402 (Interlink Electronics, 2011). The selected FSR is a miniature rounded sensor that has solder tabs for easy connection, as shown in Figure 4. Table 1 shows the characteristics of the selected FSR. The dimensions of the FSR 402 are outlined in Table 2.
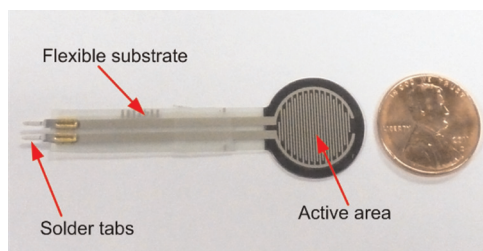

(a) (b)
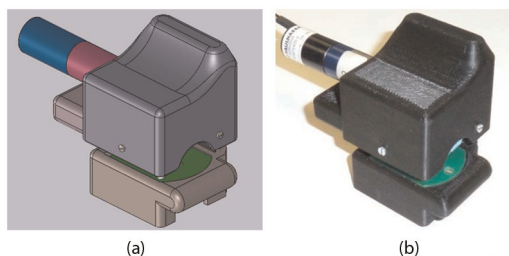
Figure 1. Finger-wearable E-Braille device: (a) model and (b) prototype.
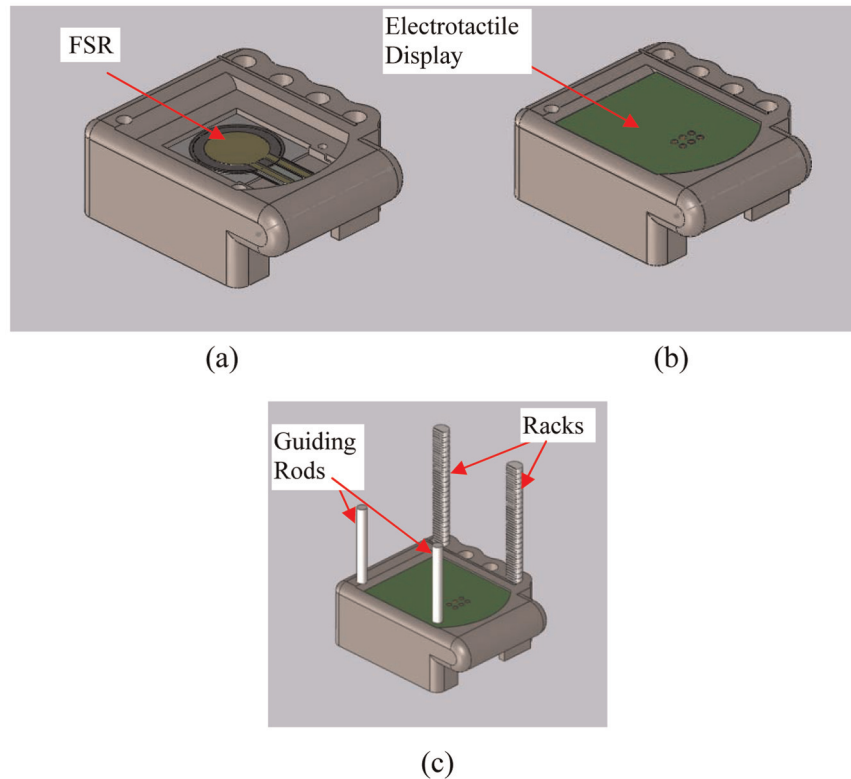
Figure 2. Setup of the electrotactile display: (a) FSR installation, (b) electrotactile display and (c) the two racks and guiding rods.
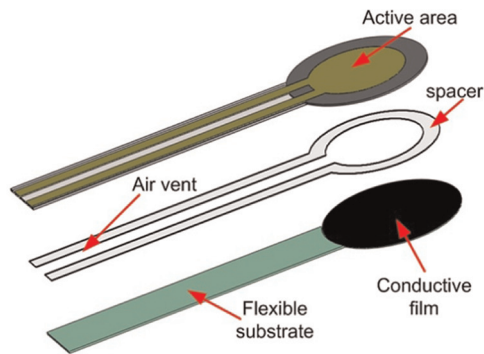
Figure 3. Typical FSR layers arrangement.
FSR: force-sensing resistor.

**Figure 4.** FSR 402.
FSR: force-sensing resistor.

An FSR works as an open circuit at no load, and when pressure is applied at its active surface, the flexible substrate deforms. This allows the top substrate to be pushed against the bottom substrate, which causes the resistance to drop. If characterized properly, this

**Table 1.** Characteristics of FSR 402 (Interlink Electronics, 2011).

Feature	Value
Wide force sensitivity range	0.1–10 N
Active area (diameter)	12.70 mm
Thickness range	0.2–1.25 mm
Stand-off resistance	>10 MΩ
Hysteresis	+ 10%
Temperature operating range	−30°C to + 70°C
Number of actuations (life time)	10 million tests

Table 2. Dimensions of the FSR 402 circular part.

Parameter	Value (mm)
Overall diameter (D_c)	18.24
Diameter of actuated area (D_{ac})	10.80
Thickness (t)	0.5334
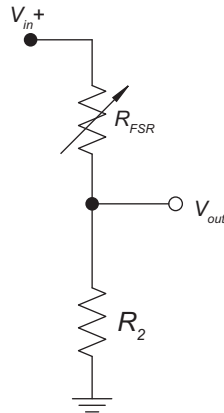
Figure 5. FSR's voltage divider.
FSR: force-sensing resistor.
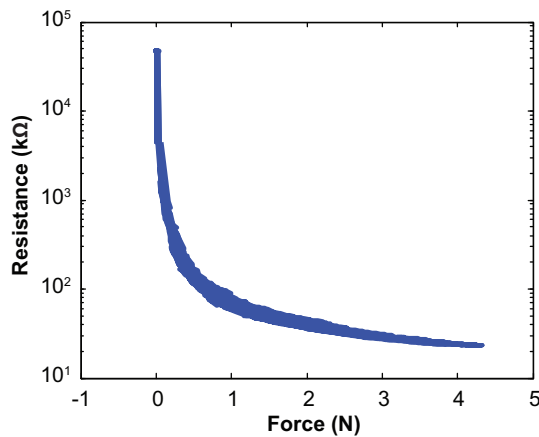
Figure 6. A typical FSR's response due to external force.
FSR: force-sensing resistor.

drop in resistance can be utilized to measure the force applied at the FSR's surface. FSRs are passive resistors that are usually configured in voltage divider circuits for simple resistance-to-voltage conversion, as shown in Figure 5.

A pressure that is applied at the FSR's surface will cause a drop in its resistance, which causes an increase in the voltage read between the circuit's terminals, as given in the following

$$V_o = V_{in}\left(\frac{R_2}{R_2 + R_{FSR}}\right) \qquad (1)$$

Depending on the application requirements, an operational amplifier can be installed at the output's terminal of the voltage divider. Figure 6 shows how the FSR's resistance drops with the application of force at its surface.

Experimental setup

An experimental procedure where the FSR is exposed to different displacement profiles is designed to identify possible models of the FSR. A component

characterization device (TestBench Instruments, 2011; Figure 7) is used throughout this study. This device has a high resolution actuator (minimum controllable displacement of 1.5×10^{-3} mm) and is equipped with a low-range (5 lbs $\approx$ 22 N) miniature load cell (Honeywell, 2011). The linear actuator is used to generate different displacement profiles to mimic various tactile forces.

A fixture is designed to ensure proper reading of the FSR (Figure 8(a)). The FSR is placed on one part of the fixture, which has a solid flat surface that is attached to the load cell through a standard threaded adapter, for an even force distribution on the FSR's active area. Double-sided adhesive is used to hold the FSR to the fixture. The second part of the fixture is attached to the end of a cylindrical actuator that applies pressure onto the FSR's active area. The FSR's terminals are connected to a voltage divider (Voltage Divider, 2011), as shown in Figure 8(b). One of the external channels of the device is used to read the voltage divider circuitry. The voltage divider has an adjustable resistance of 1–20 kΩ that can control the sensitivity of the output. A potentiometer that is integrated within the voltage divider is used to tune the resistance R_2 of Figure 5. The voltage divider is then connected to the Peripheral Component Interconnect (PCI) conditioning module via a Video Graphics Array (VGA) male connector (15-pin HD D-Sub).

To conduct the testing, we use the reaction bracket of the testing system to hold the load cell and the FSR to the testing table. This reaction bracket is equipped with a microadjuster for accurate specimen positioning. Figure 9 shows the experimental setup. At each experiment, the applied displacements, the resulting forces, and the corresponding FSR voltages are measured.

## Experimental data and signal conditioning

Tactile forces are the forces induced by a human's fingertip to recognize haptic and read Braille. In a previous study (Saadeh and Trabia, 2010), a system was developed to measure these forces. It was found that the tactile force amplitude varies among subjects, but in general it ranges between 0.2 and 3.0 N. The displacement profiles in this study are selected to represent this force range. The identification process starts by applying static displacement at the FSR's surface for an extended period ($\approx$30 min). These loads are used to calibrate the FSR and study its time drift. Results depicted in Figure 10 show that the FSR's response is fairly steady. The resistance however exhibits a small time drift (creep) in the order of $+$ 6%, which confirms the results of Florez and Velasquez (2010).

During the transition from no-load to load states, the FSR's resistance drops significantly, as illustrated in Figure 6. Proper consideration should be taken to
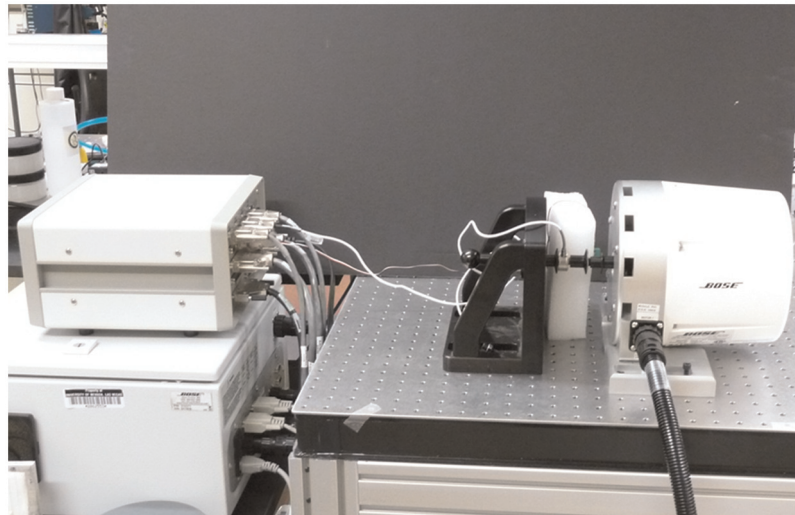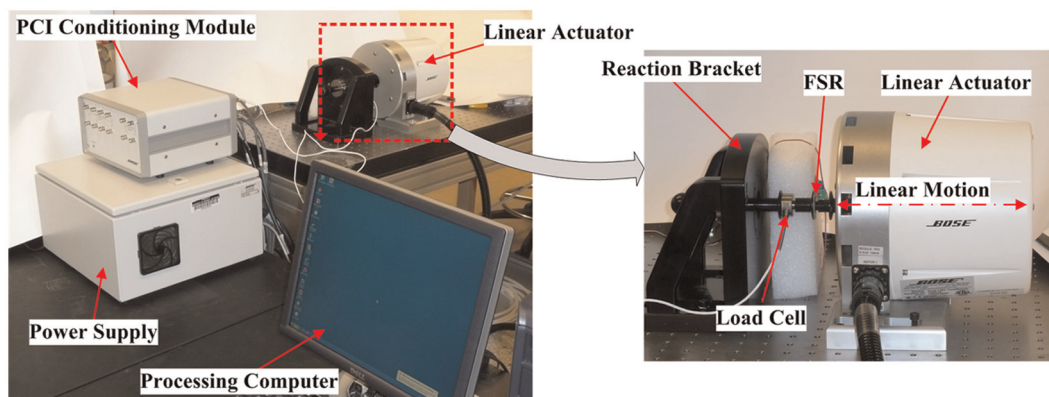
**Figure 7.** Component characterization device.
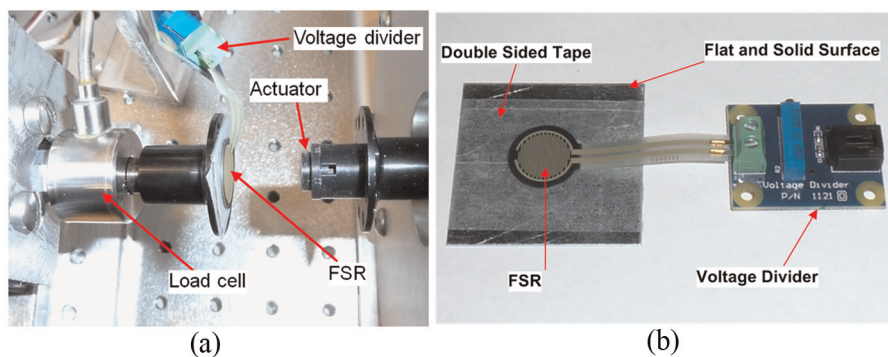
Figure 8. FSR testing fixture: (a) experimental fixture and (b) FSR interfaced with the voltage divider.
FSR: force-sensing resistor.

Figure 9. FSR experimental setup.
FSR: force-sensing resistor.

exclude this transition as it may deprive the current analysis. Thus, all data are recorded while the actuator's effector is always in physical contact with the FSR's active surface (even with the absence of external loadings). Physical equilibrium offsets appear in the data since the FSR is always under compression.
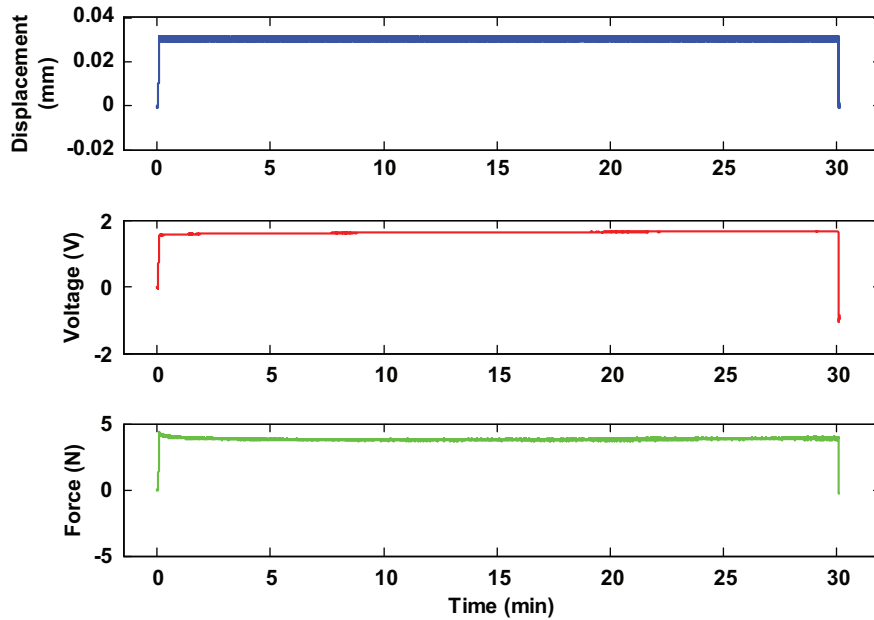
Figure 10. Results of the static loading experiment.

Therefore, all recorded profiles are detrended by removing the physical equilibrium offsets that appear before external displacements are applied. This is an essential step to estimate more accurate models (Ljung, 2011).

After calibrating the experiment, the identification process continues with the second phase to identify the dynamics of the FSR. On average, a Braille reader can read 60–120 words per minute (Mousty and Bertelson, 1985), which corresponds to 0.1–0.2 s to identify a Braille character. Hence, an up chirp sinusoidal signal (0.2–20 Hz) is applied at the FSR's surface to investigate the dynamics of the system. The chirp signal starts at a frequency of 0.2 Hz with increments of 0.1 Hz till 1.0 Hz and then with an increment of 1.0 Hz till 20 Hz, as shown in Figure 11.

All loadings are sampled at a frequency of 100 Hz. A fast Fourier transform (FFT) analysis was conducted for the FSR's voltage to determine the filtering cutoff frequency (Figure 12). Based on these results, it is determined that frequencies higher than 40 Hz should be filtered out. In addition to the chirp signal, other displacement profiles typical of tactile applications are used to assess the identification process. These profiles are square (0.1 and 0.2 Hz), triangle (0.1 and 0.2 Hz), and step (0.1 Hz).

DMA test

In the DMA test, the FSR is subjected to cyclic excitations at different frequencies to study its mechanical characteristics. The DMA is used to determine the parameters of the second-order system model of the FSR, stiffness (k), and damping (c) (Figure 13). The test monitors the displacement input and the force output and calculates the values of k and c that best fits the input and output data.

The mass m_{ac} refers only to the segment of the FSR that is actuated by the DMA test, as shown in Figure 14. To calculate this mass, we trimmed the terminals of the FSR and measured the mass of only the circular part (m_c). It is assumed that this part to be homogenous; thus, the mass of the actuated material, which has a diameter (D_{ac}), can be given as

$$m_{ac} = m_c \left(\frac{D_{ac}}{D_c}\right)^2 \qquad (2)$$

where D_c is the overall diameter of the FSR's circular part. Based on the above-mentioned analysis, the mass of circular area (m_c) is 0.1401 g and the mass of actuated area (m_{ac}) is 0.0491 g. To ensure the validity of the results, the DMA test was repeated for the same FSR (24 h later), and the results are presented in Table 3. The results of Table 3 showed that both tests generated fairly close results (the maximum difference is less than 6.5%). The data were averaged and fitted using regression analysis, and the following formulas were generated
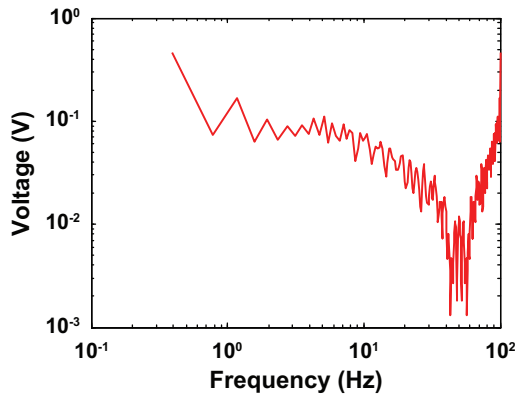
$$c = 53.96f^2 - 44.44f + 10.81 \qquad (3)$$

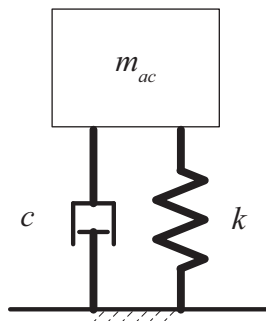$$k = 23.82f + 94.32 \qquad (4)$$

where f is the frequency of the actuation forces. Figure 15(a) and (b) shows the experimental and fitted data for the damping and stiffness, respectively.
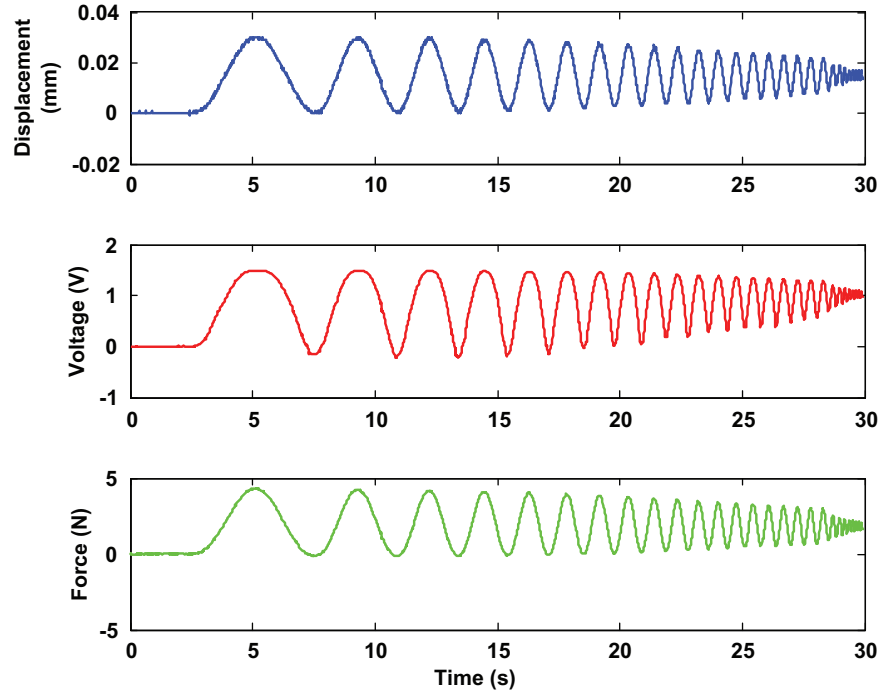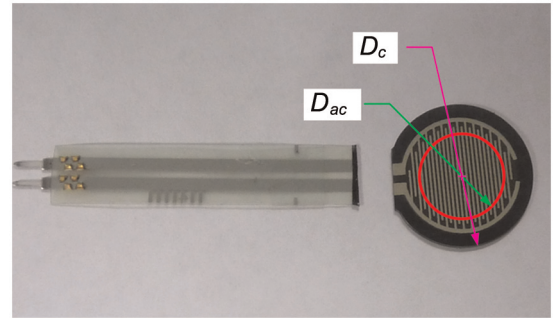
Figure 11. Dynamic loading experiment.

Figure 12. FFT analysis for the FSR voltage.
FFT: fast Fourier transform; FSR: force-sensing resistor.

Figure 13. FSR mathematical modeling.
FSR: force-sensing resistor.

Figure 14. Actuated segment of FSR.
FSR: force-sensing resistor.

The mathematical model shown in Figure 13 can be used to characterize the relation between the voltage of the FSR and the force applied at its surface. The relation between the input (displacement) and the output (force) is outlined in equation (5)

$$F = m_{ac}\ddot{y} + c\dot{y} + ky \qquad (5)$$

where F is the force applied at the FSR's surface, and y is the FSR's displacement.

It is assumed that the FSR's voltage V is proportional to y, as follows

$$V \propto y$$

Therefore, the relation between the V and F can be reached as in equation (6)

Table 3. FSR 402 mechanical properties.

Frequency (Hz)	Damping c (N s/m)		Stiffness k (kN/m)	
	Test 1	Test 2	Test 1	Test 2
0.125	6.1797	6.0950	97.32	94.81
0.250	2.8768	3.0445	102.72	101.39
0.375	1.8284	1.8667	105.07	101.69
0.500	2.0041	2.0822	106.46	104.64

Table 4. Fitness values for the second-order linear model.

Input signal	Fitness
Chirp (0.2–20 Hz)	73.46
Square (0.20 Hz)	63.85
Square (0.10 Hz)	62.81
Step (0.1 Hz)	69.55
Triangle (0.25 Hz)	74.26
Triangle (0.10 Hz)	61.40

$$F = A\left(m_{ac}\ddot{V} + c\dot{V} + kV\right) \tag{6}$$

where A is the proportionality constant.

The following performance index is used to compare the closeness of this model to the experimental results by measuring the proportion of the experimental data that can be explained by this model (goodness of fit)

$$Fitness = \left(1 - \frac{\sqrt{\sum (y_h - y)^2}}{\sqrt{\sum (y - \tilde{y})^2}}\right) \times 100\% \tag{7}$$

where y_h is the output of the proposed model, and y represents the experimental output, with $\tilde{y}$ being the mean of the experimental output.

We used one of the experimental data to test the model and calibrate the A value. For this purpose, the chirp signal of Figure 11 was selected. The optimal A value of 2.258×10^{-5} was found using Zoutendijk's feasible direction method (Rao, 2009). Table 4 shows the fitness of the proposed system under different loading inputs. Figures 16 to 21 show the results of the proposed model for various input signals.

As shown in Table 4 the proposed second-order linear model fails to satisfactorily explain the input/output relation for the loading profiles. Therefore, we investigate the possibility of obtaining a more adequate representation through the use of higher order linear and nonlinear models as presented in the next section.

Nonlinear system identification

Nonlinear systems can be modeled as cascaded blocks of a decomposed linear along with nonlinear element(s). The model can either have a static nonlinearity at the input (Hammerstein model), a static nonlinearity at the output (Wiener model), or both input and output static nonlinearities (Hammerstein–Wiener model), as shown in Figure 22. For a detailed description about these techniques, the reader is referred to Ljung (1999).

The Hammerstein model (Figure 22(a)) can be represented by the following equations

$$v(t) = F(u(t)) \tag{8}$$

$$y(t) = \frac{B(z^{-1})}{A(z^{-1})}v(t) + e(t) \tag{9}$$

On the other hand, the Wiener model (Figure 22(b)) can be represented by the following equations
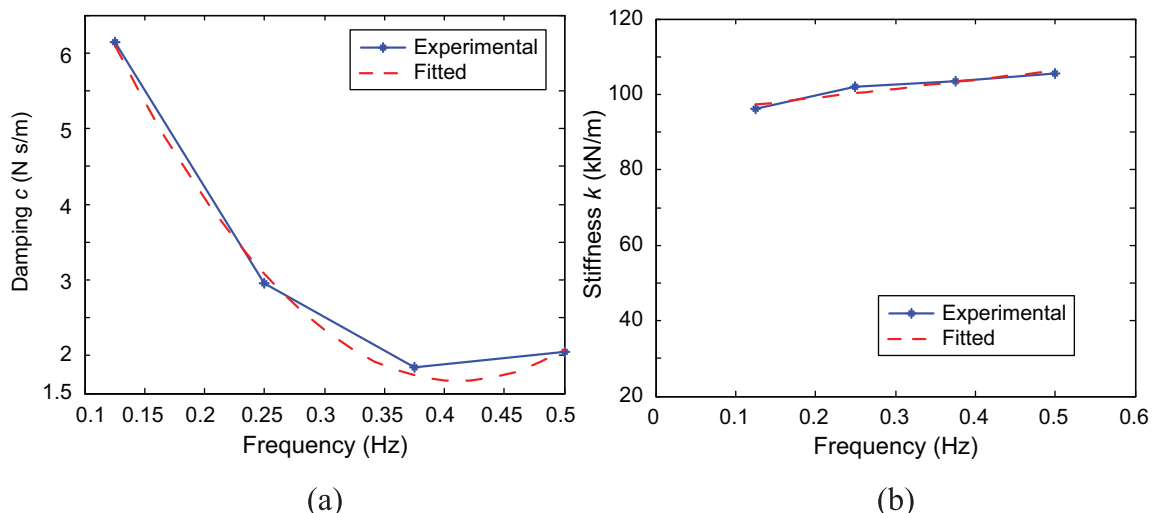
Figure 15. DMA experimental versus fitted data: (a) damping coefficient and (b) mechanical stiffness.
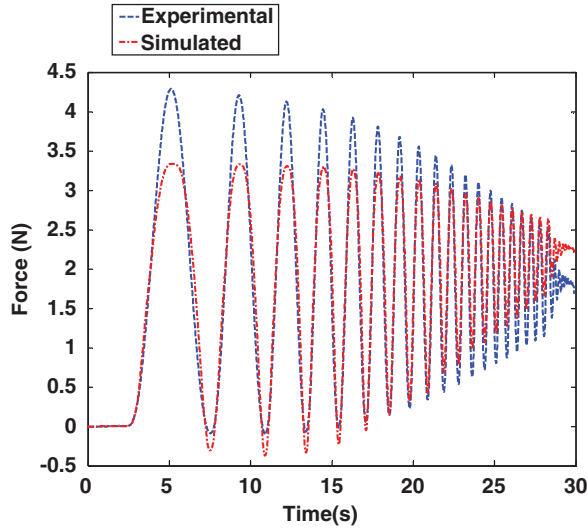DMA: dynamic mechanical analysis.
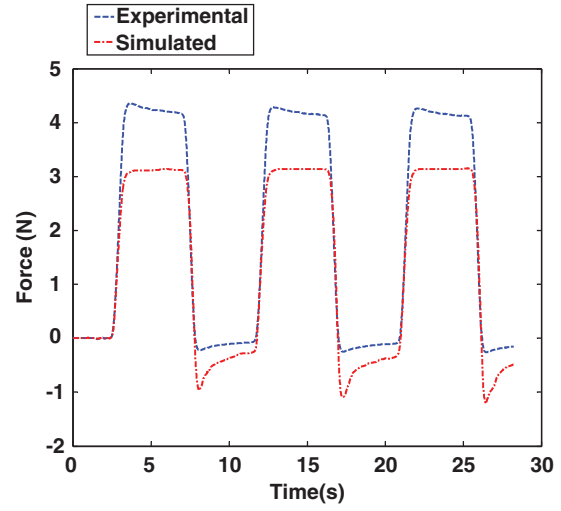
Figure 16. Chirp input signal.

Figure 18. Square signal (0.10 Hz).
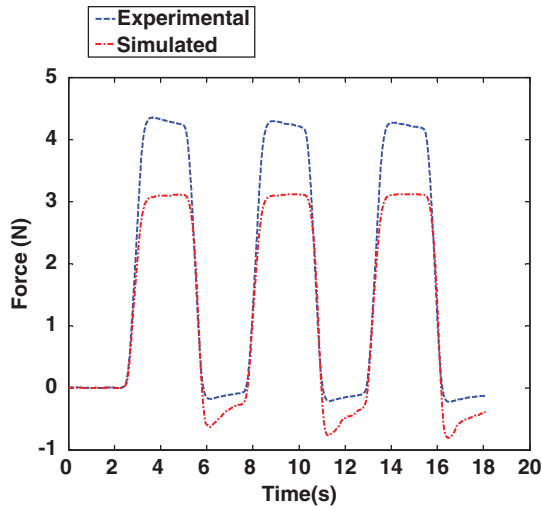
Figure 17. Square signal (0.20 Hz).
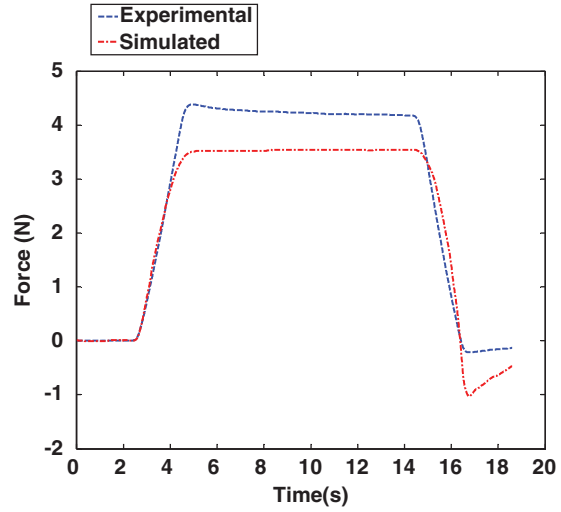
Figure 19. Step signal (0.10 Hz).

$$w(t) = \frac{B(z^{-1})}{A(z^{-1})} u(t) + e(t) \tag{10}$$

$$y(t) = G(w(t)) \tag{11}$$

where

$$A(z^{-1}) = 1 + a_1 z^{-1} + a_2 z^{-2} + \cdots + a_n z^{-n} \tag{12}$$

$$B(z^{-1}) = b_0 + b_1 z^{-1} + b_2 z^{-2} + \cdots + b_m z^{-m} \tag{13}$$

$$\begin{aligned} F(0) = G(0) = 0 \\ \forall u : |F(u)| < \infty \quad \forall w : |G(w)| < \infty \end{aligned} \tag{14}$$

where $u(t)$ and $y(t)$ are the system's input and output, respectively. The internal signals $v(t)$ and $w(t)$ are non-measurable signals. The functions $F(.)$ and $G(.)$ can be any two functions that map the input into the output

Figure 20. Triangle signal (0.25 Hz).

Figure 21. Triangle signal (0.10 Hz).

space (i.e. polynomial, piecewise, dead zone, and saturation). The nonlinear estimators are finite (Billings and Fakhouri, 1977; Giri et al., 2002), as suggested in equation (14). For 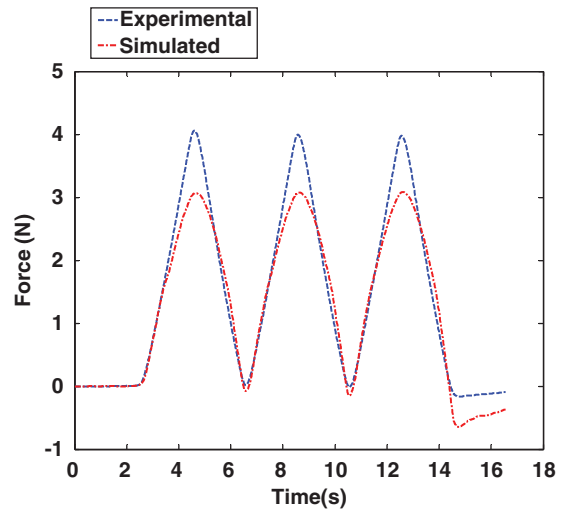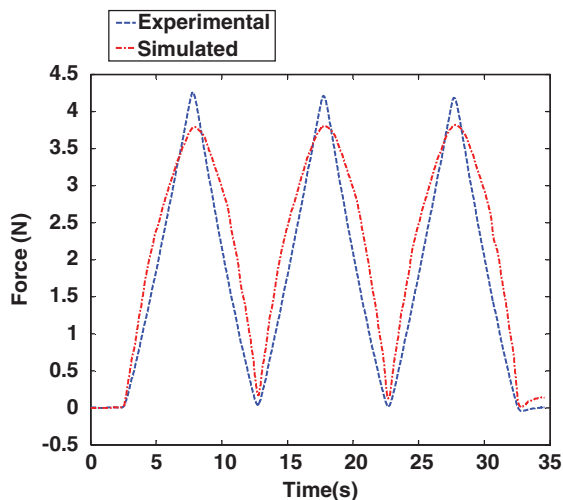instance, equation (8) maps the input $u(t)$ into the space of $v(t)$ through the nonlinear estimator function $F(.)$. Figure 23 shows a typical piecewise linear function that maps the input into the output space. If the input/output relation involves nk delay samples, then the first nk coefficients of the $B(z^{-1})$ term are zeros. For detailed identification of the Wiener and Hammerstein models, the reader is referred to Billings and Fakhouri (1977) and Giri et al. (2002), respectively.

Comparison of linear and nonlinear models of the FSR

Proposed approach

Four models of interest are developed and compared. These models are a linear model, Hammerstein,
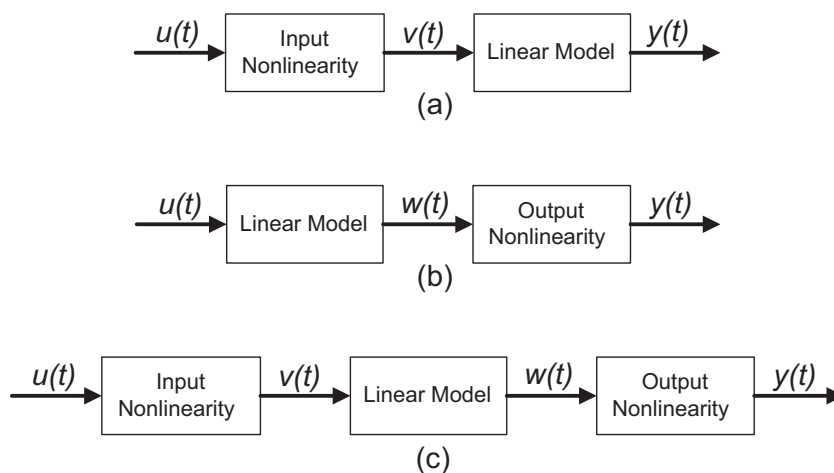
Wiener, and Hammerstein–Wiener nonlinear models. The accuracy and robustness of these four models are assessed using various loading profiles. The proposed models are created using the System Identification Toolbox of MATLAB® (Ljung, 2011).

Linear system identification

In this study, the identification process follows these steps. First, using the chirp input signal (Figure 11), we gradually increase the order of the linear system until the results of the fitness function (equation (7)) cannot be further improved significantly (Eskinat et al., 1991). The results of this process (Table 5) are generally better than those of Table 6. These results indicate that the performances of all linear models are extremely close to each other. The results of this section and the previous one indicate that a linear model alone is not sufficient to model the signal. Thus, it is decided to assess the effect of using linear systems in conjunction with nonlinear terms, as shown in the next section. Appendix 1 lists the parameters of the identified linear systems.

Nonlinear system identification

The process continues with identifying the input and output nonlinearities for the Hammerstein, Wiener, and Hammerstein–Wiener models. It is decided to use piecewise linear function breakpoints in equations (8) and (11). Extensive testing shows that using a piecewise linear function with four breakpoints is sufficient to estimate the static nonlinearities in these three models. Similar to the previous section, the chirp signal is used to identify the parameters of the linear and nonlinear components of the three nonlinear models. Appendices 2 and 3 list the parameters of the identified linear parameters and the input/output pairs of the nonlinear blocks, respectively.

Figure 22. (a) Hammerstein model, (b) Wiener model, and (c) Hammerstein–Wiener model.

The fitness values for simulating different loadings using the Hammerstein, Wiener, and Hammerstein–Wiener models are shown in Tables 6 to 8, respectively. Table 6 shows that it is difficult to decide which model order produces the best results in the Hammerstein model, as the best fitness values are not clustered at one order. Furthermore, the results of the Hammerstein model do not improve steadily with increasing the order of the linear system. Table 7 demonstrates that the overall performance of the Wiener model improves with increasing the order of the linear system. A fifth-order linear system can describe more signal data than any other lesser order systems in the Wiener model. Similar to the Hammerstein model, one cannot decide which system's order generates the best results in the Hammerstein–Wiener model, as illustrated in Table 8. In fact, the results of both the third-order and fifth-order linear systems are close to each other. However, the results of the Wiener model surpass all other results. Thus, the results suggest that a fifth-order Wiener model produces the best fitness values for the tested signals. This model is able to effectively describe most of the loading profiles to very satisfactory levels. Figures 24 to 29 show the results of the proposed models for various input signals.

The best improvement in the overall fitness results for the Wiener model was achieved when the order of the linear system increased from second to fifth, as shown in Table 7. For example, in the triangle 0.1-Hz signal case, the fitness of the second-order model was about 50%. This fitness was improved to 87% when a
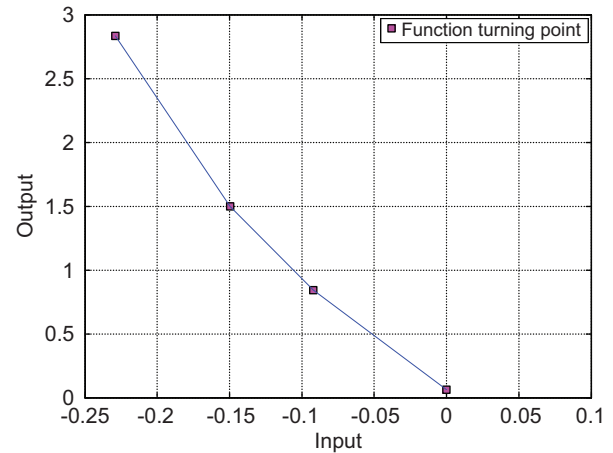
Figure 23. Piecewise output nonlinearity estimator.

fifth-order system was used. As the order of the system increased, the observed overall improvement was not associated with significant change in the computational effort. In fact, any order of the proposed models can be represented as a linear system followed by a piecewise function to map the output into a different domain. Thus, increasing the order of the linear system will only result in a modified mathematical expression with no need for additional expressions/blocks to account for the increase in the linear model's order. The model can be installed on a microcontroller for real-time applications, where the microcontroller processes the voltage signal received from the FSR to compute the actual applied force.

Table 5. Fitness values for the linear model of second order through fifth order.

Input signal	Linear system order			
	Second order	Third order	Fourth order	Fifth order
Chirp (0.2–20 Hz)	78.79	78.85	78.92	78.93
Square (0.20 Hz)	81.86	83.12	81.89	81.89
Square (0.10 Hz)	81.93	83.28	82.12	82.10
Step (0.1 Hz)	76.25	77.87	76.62	76.59
Triangle (0.25 Hz)	76.51	77.84	76.79	76.78
Triangle (0.1 Hz)	65.52	69.17	66.14	66.09

Table 6. Fitness values for the Hammerstein model.

Input signal	Linear system order			
	Second order	Third order	Fourth order	Fifth order
Chirp (0.2–20 Hz)	90.87	95.89	91.20	91.84
Square (0.20 Hz)	85.59	79.15	83.33	86.52
Square (0.10 Hz)	89.90	90.31	87.90	90.92
Step (0.1 Hz)	83.01	83.98	86.17	81.50
Triangle (0.25 Hz)	86.69	79.40	84.96	87.47
Triangle (0.1 Hz)	65.44	43.44	69.43	63.20

Table 7. Fitness values for the Wiener model.

Input signal	Linear system order			
	Second order	Third order	Fourth order	Fifth order
Chirp (0.2–20 Hz)	95.23	95.47	88.96	93.46
Square (0.20 Hz)	76.98	84.16	91.50	93.02
Square (0.10 Hz)	77.67	84.52	92.67	93.52
Step (0.1 Hz)	89.54	94.84	92.82	95.01
Triangle (0.25 Hz)	78.87	85.51	91.03	92.36
Triangle (0.1 Hz)	49.82	62.08	82.02	87.25

Table 8. Fitness values for the Hammerstein–Wiener model.

Input signal	Linear system order			
	Second order	Third order	Fourth order	Fifth order
Chirp (0.2–20 Hz)	95.89	94.46	83.87	84.53
Square (0.20 Hz)	79.15	82.11	71.47	83.58
Square (0.10 Hz)	79.71	82.79	76.58	84.15
Step (0.1 Hz)	83.98	94.50	89.07	92.83
Triangle (0.25 Hz)	79.40	79.78	73.32	82.68
Triangle (0.1 Hz)	43.44	62.04	63.26	75.93
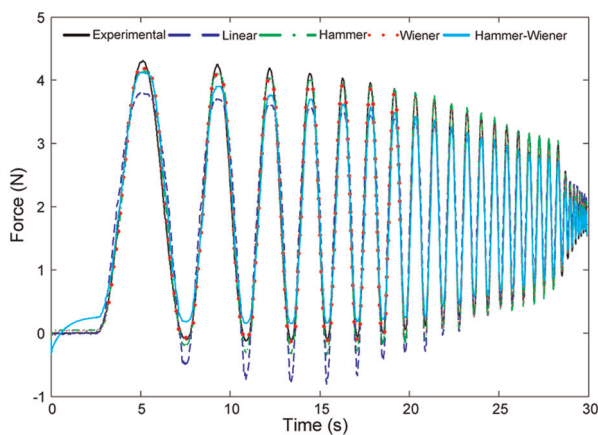
Figure 24. Chirp input signal.
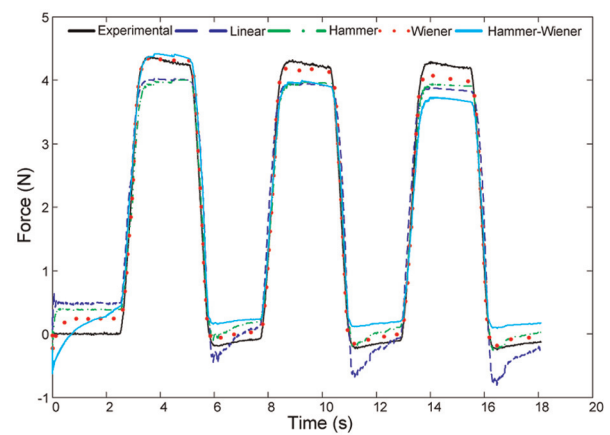
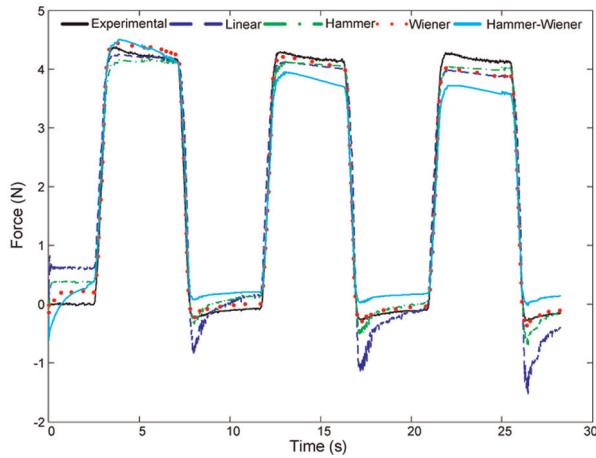
Figure 25. Square input signal (0.20 Hz).

The Wiener model, which outperformed all other proposed systems, assumes nonlinearity to exist only on the output side. This arrangement seems to be more suited for this application as adding nonlinearity at the input stage will map the voltage signal into a different domain, thus forming regions with different characteristics within the voltage signal. Although these regions are continuous at the connection points, the areas surrounding these points will generate different outputs where changes in amplitude/shapes of the output signal may be noticed. A slight disturbance in the voltage signal in these areas may result in a bigger and sudden change in the force output, which will not match the profile of the applied force signal. In addition, the

FSR's resistance–voltage relation is defined using a simple linear formula (equation (1)). The voltage signal is directly proportional to the inverse of the sensor's resistance, and it serves as a direct indication for the drop in the resistance; thus, no mapping is needed at the input signal side.
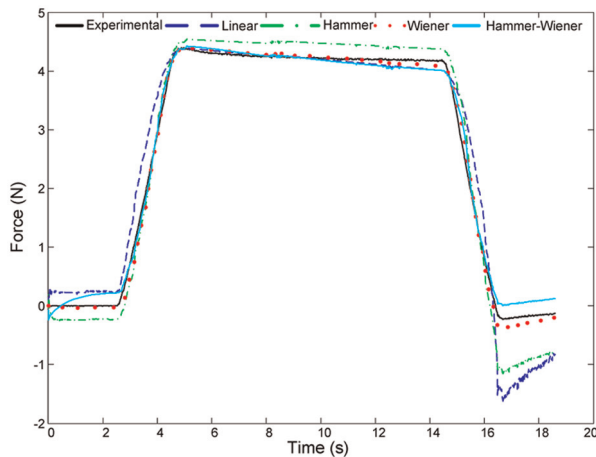
Conclusion

FSRs can be an attractive option to traditional force-sensing applications, especially when the cost and space are concerned. To effectively utilize FSRs, an accurate model that can describe their behavior under different conditions is needed. This study presents a method for
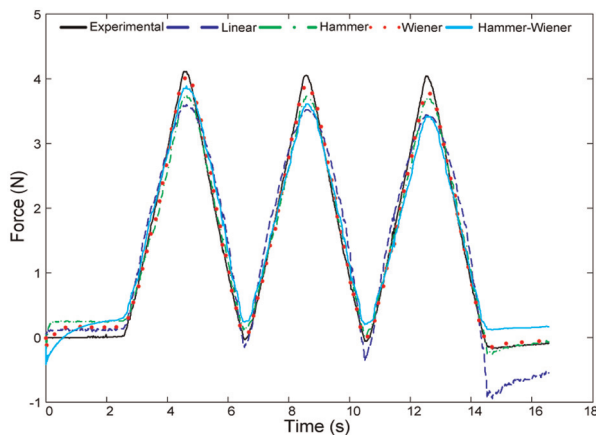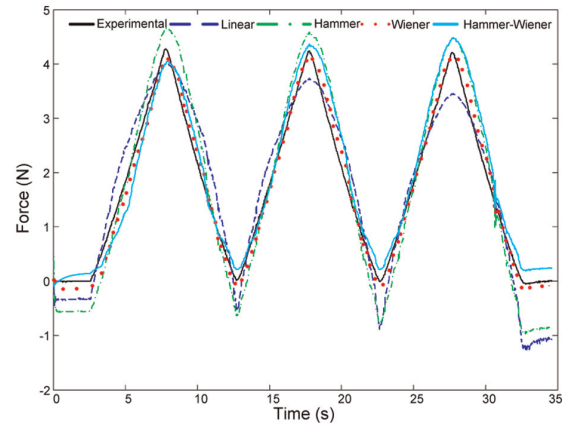
Figure 26. Square input signal (0.10 Hz).

Figure 27. Step input signal (0.10 Hz).

Figure 28. Triangle input signal (0.25 Hz).

Figure 29. Triangle input signal (0.10 Hz).

second-order system where the stiffness and damping are frequency-dependent values. These values are obtained using DMA test. This linear model does not generate satisfactory results as it describes only the linear behavior of the FSR. Higher order (second through fifth) linear models are generated using system identification techniques. The same chirp signal is used as an input for all these models. With increasing the order of the linear model, the simulation results of these models were improved only slightly. This suggested that linear models alone (regardless of their order) are insufficient to describe the behavior of the FSR, and that nonlinear terms need to be considered. Both the Hammerstein and Wiener models combine linear and nonlinear behaviors of the same signal. They provide simple techniques to model these nonlinearities through incorporating cascaded linear and nonlinear blocks. Three models are considered in this study: Hammerstein, Wiener, and Hammerstein–Wiener. A piecewise linear function with four breakpoints is used to model the static nonlinearities in the Hammerstein, Wiener, and Hammerstein–Wiener models. It is shown that the performance of a nonlinear model is a function of several factors as the loading profile, the order of the linear system, and the nonlinear element estimator used. However, the overall performance of a Wiener model of fifth order surpasses the other models.

identifying a model for FSRs using a component characterization device. A fixture is customized to allow proper testing of the FSR. The FSR is modeled as a

References

Billings S and Fakhouri S (1977) Identification of nonlinear systems using the Wiener model. *Electronics Letters* 13(17): 502–504.

Birglen L and Gosselin C (1995) Fuzzy enhanced control of an underactuated finger using tactile and position sensors. In: *Proceedings of the IEEE international conference*, Barcelona, Spain, 18–22 April 2005, pp. 2320–2325.

Eskinat E, Johnson S and Luyben W (1991) Use of Hammerstein models in identification of nonlinear systems. *AIChE Journal* 37(2): 255–267.

Florez J and Velasquez A (2010) Calibration of force sensing resistors (FSR) for static and dynamic applications. In: *2010 IEEE ANDESCON*, Medellin, Colombia, 15–17 September 2010, pp. 1–6.

Giri F, Chaoui F, Haloua M, et al. (2002) Hammerstein model identification. In: *Proceedings of the 10th Mediterranean conference on control and automation—MED2002*, Lisbon, Portugal, 9–12 July 2002.

Hall R, Desmoulin G and Milner T (2008) A technique for conditioning and calibrating force-sensing resistors for repeatable and reliable measurement of compressive force. *Journal of Biomechanics* 41: 3492–3495.

Hollinger A and Wanderely M (2006) Evaluation of commercial force-sensing resistors. In: *The 6th international conference on new interfaces for musical expression NIME06*, Paris, France, 4–8 June 2006.

Honeywell (2011) Model 31 Low. Available at: https://measurementsensors.honeywell.com/ProductDocuments/Load/Model_31_Datasheet.pdf (accessed 21 October 2011).

Interlink Electronics (2011) FSR 402. Available at: http://www.steadlands.com/data/interlink/fsr402.pdf (accessed 14 October 2012)

Jensen T, Radwin R and Webster J (1991) A conductive polymer sensor for measuring external finger forces. *Journal of Biomechanics* 24(9): 851–858.

Lebosse C, Bayle B, Mathelin M, et al. (2008) Nonlinear modeling of low cost force sensors. In: *IEEE international conference on robotics and automation*, Pasadena, CA, 19–23 May 2008, pp. 3437–3442.

Ljung L (1999) *System Identification: Theory for the User*. Englewood Cliffs, NJ: Prentice Hall-PTR, ch. 5.

Ljung L (2011) *System Identification Toolbox 7: User's Guide*. Natick, MA: MathWorks, Inc.

Mousty P and Bertelson P (1985) A study of braille reading: 1. Reading speed as a function of hand usage and context. *Quarterly Journal of Experimental Psychology Section A: Human Experimental Psychology* 37: 217–233.

Rao S (2009) *Engineering Optimization: Theory and Practice*. 4th ed. Hoboken, NJ: Wiley.

Saadeh M and Trabia M (2010) Development of a measuring system of contact force for braille reading using a six-axis force sensor. In: *International mechanical engineering congress and exposition IMECE2010*, Vancouver, BC, Canada, 12–18 November 2010, No. 39976.

Saadeh M, Trabia M, Shen Y, et al. (2010) Design of a wearable fingertip haptic braille device. In: *Proceedings of the 2010 design of medical devices conference DMD2010*, Minneapolis, MN, 13–15 April 2010, No. 3873.

TestBench Instruments (2011) Available at: http://www.bose-electroforce.com/products/specs/TestBenchSeries.pdf (accessed 21 November 2011).

Vaidyanathan C and Wood H (1991) An expert system based modeling scheme for tactile data interpretation. *Robotics and Autonomous Systems* 8: 213–237.

Vecchi F, Freschi C, Micera S, et al. (2000) Experimental evaluation of two commercial force sensors for applications in biomechanics and motor control. In: *Proceedings of the 5th annual conference of the international functional electrical stimulation society IFESS2000*, Aalborg, Denmark, 18–24 June 2000.

Voltage Divider (2011) Available at: http://www.phidgets.com/products.php?category=1&;product_id=1121_0 (accessed 10 October 2011).

Zehr E, Stein R, Komiyama T, et al. (1995) Linearization of force sensing resistors (FSR's) for force measurement during gait. In: *IEEE-EMBC and CMBEC, theme 7: instrumentation*, 20–23 September 1995, pp. 1571–1572.

Appendix 1

Parameters of the identified linear systems

	b_0	b_1	b_2	b_3	b_4	a_1	a_2	a_3	a_4	a_5
Second order	5.184	−5.184				−0.001	−0.999			
Third order	5.300	−10.546	5.246			−0.990	−0.998	0.988		
Fourth order	6.122	−9.867	3.963	−0.218		−0.644	−0.850	0.639	−0.145	
Fifth order	8.591	−20.301	19.425	−8.932	1.216	−0.543	−1.340	1.072	0.360	−0.549

Appendix 2
Parameters of the identified nonlinear systems

		b_0	b_1	b_2	b_3	b_4	a_1	a_2	a_3	a_4	a_5
Second order	Hammer	−1.000	1				−0.006	−0.994			
	Wiener	−1.006	1				0.005	−0.991			
	Hammer–Wiener	−1.006	1				−0.067	−0.920			
Third order	Hammer	−0.503	1	−0.497			−0.990	−0.998	0.988		
	Wiener	−0.506	1	−0.494			−0.978	−0.994	0.972		
	Hammer–Wiener	−0.514	1	−0.486			−1.326	−0.249	0.576		
Fourth order	Hammer	−0.951	1	0.375	−0.423		−0.065	−1.323	0.062	0.326	
	Wiener	−0.872	1	0.166	−0.294		−0.180	−1.210	0.178	0.212	
	Hammer–Wiener	−0.341	1	−0.977	0.318		−1.938	−0.039	1.893	−0.916	
Fifth order	Hammer	−0.562	1	−0.428	0.004	−0.014	−0.479	−1.450	0.614	0.475	−0.159
	Wiener	−0.529	1	−0.631	0.339	−0.179	−0.264	−1.558	0.176	0.581	0.065
	Hammer–Wiener	−1.157	1	1.208	−0.828	−0.222	0.271	−1.848	−0.656	0.853	0.380

Appendix 3
Input/output pairs of the nonlinear blocks

		Input nonlinearity				Output nonlinearity			
		N pairs				N pairs			
Second order	Hammer	0.143	0.479	0.833	1.150				
		−0.506	−1.776	−3.315	−5.176				
	Wiener					−0.628	−0.472	−0.301	−0.002
						3.431	2.163	1.157	0.087
	Hammer–Wiener	0.457	0.789	0.869	1.145	−1.305	−0.814	−0.577	0.103
		1.236	1.789	1.891	2.243	3.620	1.301	0.724	0.058
Third order	Hammer	0.136	0.476	0.817	1.157				
		−1.192	−3.940	−6.976	−10.964				
	Wiener					−0.293	−0.189	−0.132	−0.001
						3.083	1.585	1.018	0.102
	Hammer–Wiener	−0.184	0.484	0.791	1.216	−0.049	−0.039	0.005	0.141
		−0.708	−0.049	0.139	0.316	1.507	1.288	0.761	0.063
Fourth order	Hammer	0.136	0.475	0.817	1.155				
		−0.708	−2.288	−4.116	−6.560				
	Wiener					−0.419	−0.286	−0.155	−0.020
						2.804	1.597	0.768	0.123
	Hammer–Wiener	0.139	0.505	0.788	1.158	−0.115	−0.013	0.016	0.085
		0.161	0.491	0.788	1.162	1.329	0.367	0.333	0.261
Fifth order	Hammer	0.134	0.477	0.816	1.158				
		−1.054	−3.710	−6.964	−11.386				
	Wiener					−0.229	−0.149	−0.092	0.000
						2.834	1.496	0.843	0.063
	Hammer–Wiener	0.135	0.465	0.804	1.159	−0.073	−0.053	0.001	0.042
		0.039	0.106	0.160	0.213	1.354	0.903	0.267	0.172